

Containerless Undercooled Melts: Ordering, Nucleation, and Dendrite Growth



DIETER M. HERLACH, SVEN BINDER, PETER GALENKO, JAN GEGNER,
DIRK HOLLAND-MORITZ, STEFAN KLEIN, MATTHIAS KOLBE,
and THOMAS VOLKMANN

Electromagnetic and electrostatic levitation are applied to containerless undercool and solidify metallic melts. A large undercooling range becomes accessible with the extra benefit that the freely suspended drop is accessible directly for in situ observation. The short-range order in undercooled melts is investigated by combining levitation with elastic neutron scattering and X-ray scattering using synchrotron radiation. Muon Spin Rotation (μ SR) experiments show magnetic ordering in deeply undercooled $\text{Co}_{80}\text{Pd}_{20}$ alloys. The onset of magnetic ordering stimulates nucleation. Results on nucleation undercooling of zirconium are presented showing the limit of maximum undercoolability set by the onset of homogeneous nucleation. Metastable phase diagrams are determined by applying energy-dispersive X-ray diffraction of Ni-V alloys with varying concentration. Nucleation is followed by crystal growth. Rapid dendrite growth velocity is measured on levitation-processed samples as a function of undercooling ΔT by using high-speed video camera technique. Solute trapping in dilute solid solutions and disorder trapping in intermetallic compounds are experimentally verified. Measurements of glass-forming Cu-Zr alloy show a maximum in the $V(\Delta T)$ relation that is indicative for diffusion-controlled growth. The influence of convection on dendrite growth of $\text{Al}_{50}\text{Ni}_{50}$ is shown by comparative measurements of dendrite growth velocity on Earth and in reduced gravity. Eventually, faceting of a rough interface by convection is presented as observed on Ni_2B alloys.

DOI: 10.1007/s11661-015-3052-8

© The Minerals, Metals & Materials Society and ASM International 2015

I. INTRODUCTION

METALLIC materials are prepared from the liquid state as their parent phase. To date, efforts are directed toward virtual material design with computer-assisted modeling. Computational materials science from the liquid state requires detailed knowledge of the physical mechanisms involved in the solidification process. In particular, these are crystal nucleation and crystal growth. Both of these processes are driven by an undercooling of the liquid below its equilibrium melting temperature to develop conditions where a driving force for the formation of supercritical nuclei and the advancement of a solidification front is created. This gives access to non-equilibrium solidification pathways, which can form metastable solids, which may differ in their physical and chemical properties from their stable counterparts.

Detailed modeling of solidification, far away from thermodynamic equilibrium, requires that the solidification process has to be investigated in every detail.

In order to achieve the state of an undercooled melt, it is advantageous to remove heterogeneous nucleation sites which otherwise limit the undercoolability. To achieve the state of a deeply undercooled melt, heterogeneous nucleation has to be reduced as far as possible. There are different experimental techniques to realize such conditions. Turnbull used the method of volume separation of heterogeneous sites by sample subdivision into many small particles in order to isolate the heterogeneous sites in a few particles.^[1] Later on, this technique has been refined by Perepezko by subdividing the macroscopic melt in an inert carrier fluid that may act as an agent removing heterogeneous sites on the surface of the small droplets as well.^[2] Even undercooling of macroscopic melts in a fluxing agent can be used to achieve very large undercoolings up to the glass transition temperature as demonstrated by Kui, Greer, and Turnbull. They were able to produce the first bulk metallic glass of a $\text{Pd}_{40}\text{Ni}_{40}\text{P}_{20}$ alloy by embedding the metallic melt in slice of cm into a B_2O_3 fluxing agent.^[3] In fact these measurements were later on confirmed and this technique was used to study the transformation kinetics of this alloy as a function of undercooling and cooling rate.^[4]

Containerless processing is an efficient experimental tool that provides freely suspended droplets in size of several millimeters.^[5] In such, the most dominant

DIETER M. HERLACH, Full Professor in Physics, is with the Ruhr-University Bochum, Bochum, Germany, and also Group Leader with the Institut für Materialphysik im Weltraum, Deutsches Zentrum für Luft- und Raumfahrt DLR, 51170 Köln, Germany. Contact e-mail: dieter.herlach@dlr.de SVEN BINDER, JAN GEGNER, DIRK HOLLAND-MORITZ, STEFAN KLEIN, MATTHIAS KOLBE, and THOMAS VOLKMANN, Post-doctoral Researchers, are with the Institut für Materialphysik im Weltraum, Deutsches Zentrum für Luft- und Raumfahrt DLR. PETER GALENKO, Lecturer and Post-doctoral Researcher, is with the Otto-Schott-Institut für Materialforschung, Friedrich-Schiller-Universität, Jena, Germany.

Manuscript submitted September 10, 2014.

Article published online August 15, 2015

heterogeneous nucleation process, involving interaction with container walls, is completely avoided. Electromagnetic^[6] and electrostatic levitation techniques^[7,8] have been developed for containerless undercooling and solidification of molten metals and alloys. A freely suspended drop gives the extra benefit to directly observe the solidification process by combining the levitation technique with proper diagnostic means.^[9,10] Short-range ordering in undercooled metallic melts as precursor of crystal nucleation has been investigated by using neutron diffraction^[11] and synchrotron radiation^[12] on containerless undercooled melts.^[13] In particular containerless processing under ultra-high vacuum condition is favorable to achieve large undercoolings from which the interfacial energy between crystal nucleus and undercooled melt may be inferred. Rapid growth of dendrites is observed on levitation undercooled melts by using video camera techniques characterized by high spatial and temporal resolution.^[14] During crystallization of a melt the heat of crystallization is released that leads to a temperature rise during the initial solidification. In case of containerless processing, heat is transferred by heat radiation and additionally by heat conduction in an environmental gas if the sample is processed in an inert noble gas atmosphere [*e.g.*, in electromagnetic levitation (EML)]. If the sample is undercooled prior to solidification, the initial crystallization process is very rapid. As a consequence, the undercooled melt serves as a heat sink. This leads to a temperature rise during the initial crystallization of the sample known as recalescence.

By analyzing measured temperature–time profiles and measurements of the dendrite growth velocity as a function of undercooling, non-equilibrium effects like solute trapping and disorder trapping are investigated on solid solutions and intermetallic compounds, respectively. Dendrite growth is controlled by heat and mass redistribution. Thus, any transport process stimulated externally by natural convection and/or forced convection due to stirring effects of alternating electromagnetic fields in EML experiments may cause serious influence on the solidification process. To understand this effect and to develop a quantitative description of crystallization in the presence of forced convection comparative experiments on Earth and in reduced gravity are of great help. Under the special conditions of reduced gravity, for instance in Space, the forces needed to compensate disturbing accelerations are about three orders of magnitude smaller than the forces needed to compensate the gravitational force for levitation experiments on Earth. In a cooperative effort by the European Space Agency (ESA) and the German Space Center—Space Management (DLR), a facility for EML was constructed and was accommodated on board the International Space Station (ISS) in July 2014. International research teams prepared experiments using the EML multiuser facility for investigations on undercooled metallic melts in Space.^[15]

The present article aims to give an overview of the present state of investigations in containerless undercooled melts and its solidification initiated by the nucleation process and completed by subsequent crystal growth. In case of undercooled melts of pure metals,

alloys of solid solutions, and intermetallic compounds, crystal growth is occurring as dendritic crystallization.

II. EXPERIMENTAL DETAILS

Samples were prepared from alloy constituents, all of purity of 4N5. The constituents of the alloys are pre-melted in an arc furnace under high purity argon gas (6N). The samples were placed in the ultra-high vacuum chambers of electromagnetic and/or electrostatic levitators. The temperature is measured by pyrometers with an absolute accuracy of ± 5 K. Samples in diameter of 7 mm are processed by EML. The application of EML is limited since levitation force and inductive heating is coupled. In order to cool the liquid sample, forced convection by helium gas is used. In the electrostatic levitator, samples of diameter 2 mm are processed under ultra-high vacuum conditions ($\approx 10^{-8}$ mbar). Levitation and heating is decoupled in contrast to the electromagnetic levitator. A high-speed video camera (Photron VKT) was applied (frame rate up to 50,000 pictures per second) to measure the rapid dendrite growth velocity as a function of undercooling. The measurements of dendrite growth in undercooled melts of $\text{Al}_{50}\text{Ni}_{50}$ and Ni_2B alloys in reduced gravity were conducted using the TEMPUS facility^[16] during parabolic flight campaigns. Neutron scattering experiments were performed at the Institut Laue Langevin, Grenoble (France), X-ray diffraction experiments at the Advanced Photon Source, Chicago (USA), energy-dispersive X-ray diffraction at the European Synchrotron Radiation Facility Grenoble (France) and at DESY Hamburg, and Muon Spin Rotation experiments at the Paul Scherrer Institute Villigen (Switzerland).

III. RESULTS AND DISCUSSIONS

A. Structural Short-Range Order

The structure factor of undercooled melts of pure metals as Ni, Fe, Zr,^[11] and Co^[17] was measured in the stable regime and below T_L at undercoolings up to 140 K (140 °C) for Fe and even to 290 K (17 °C) for Ni and Zr. This corresponds to high relative undercoolings ($\Delta T/T_L = (T_L - T)/T_L$) especially in the case of Ni (17 pct). Such a large temperature range should allow one to evidence significantly the structural changes occurring in the liquid $S(q)$. For example, Figure 1 shows the measured structure factor at a temperature of $T = 1453$ K (1180 °C) (solid circles) that is 276 K (276 °C) below the melting temperature. A shoulder on the right-hand side of the second oscillation is observed. This shoulder is characteristic of a particular short-range order (SRO). Such a feature has been identified as a signature of icosahedral short-range order (ISRO) from the theoretical work of Sachdev and Nelson^[18] and was recently evidenced in quasicrystal-forming alloy melts.^[19] This feature becomes more pronounced as T is lowered and undercooling is increased. Interatomic distances and coordination

numbers are quantitative parameters of SRO obtained from the corresponding pair correlation functions $g(R)$. The nearest neighbor distance, R_1 , remains essentially unchanged, while the second neighbor distance, R_2 , slightly decreases with decreasing T . The nearest neighbor coordination number, $Z \approx 12$ is obtained by the area under the first maximum of $4\pi\rho R^2g$ (ρ denotes the mass density). It was determined by integration over the whole area between first and second minima limiting this first oscillation. The Z values ($Z \approx 12$) obtained are characteristic of several types of densely packed SRO, e.g., icosahedral, fcc, and hcp.

For analysis of the measured structure factor an approach was used to simulate the structure factor $S(Q)$ for large Q values. It is based on the assumption that aggregates of specific structure are present which do not interact with each other. It implies that there are only three free fit parameters to discriminate between the different geometries of aggregates: bcc, fcc, hcp, icosahedral, and dodecahedral. The simulation method is outlined in detail in Reference 19. The parameters of the simulation are the shortest mean distance, $\langle r_o \rangle$, of atoms contained in a cluster, its mean thermal variation, δr , that determines the Debye–Waller factor, $\exp(-\langle \delta r_i^2 \rangle)$, and the concentration, X , of cluster atoms in the liquid. The mean thermal variations of the other intra-cluster distances, $\langle r_i \rangle$, are estimated by $\langle \delta r_i^2 \rangle = \langle \delta r_o^2 r_i^2 / r_o^2 \rangle$. The parameters are adjusted such that a good fit of the experimentally determined $S(Q)$ is obtained especially at high Q values. The large Q part of $S(Q)$ is determined by the SRO only as far as the contribution of larger distances is damped by thermal motions.

The results of simulations for liquid Ni in the undercooled regime at $T = 1435$ K (1162 °C) for differently structured aggregates are presented in Figure 1. For a SRO of bcc- and hcp-like structure, it is not possible to achieve a reasonable fit of the measured $S(Q)$. The best fit is obtained for icosahedral-like SRO. In particular, the assumption of ISRO can better reproduce the large oscillation at about 55 Å and the

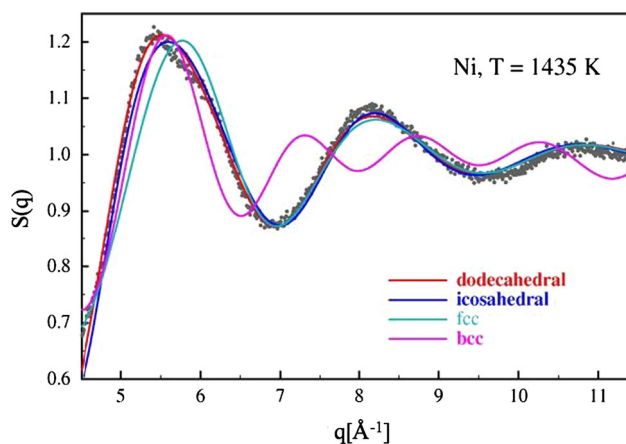


Fig. 1—Structure factor $S(q)$ measured by elastic neutron scattering on levitation undercooled Ni sample at a temperature $T = 1435$ K (1162 °C), that corresponds to an undercooling of 286 K (286 °C). Circles represent experimental data, lines give the results of simulations assuming bcc, fcc, icosahedral, and dodecahedral short-range order, respectively (Color figure online).

presence of the characteristic shoulder as an asymmetry on the right-hand side of this oscillation.

We have been dealing up to here with isolated 13 atom aggregates, but we may wonder about the nature of SRO at larger distances. A simulation based on a larger cluster, the dodecahedron, was performed. The dodecahedron is an aggregate of higher order consisting of 33 atoms, which can be constructed from the icosahedron by placing atoms densely on all its 20 triangular faces. When comparing the results obtained for the two clusters with icosahedral symmetry, it is obvious that the assumption of dodecahedral aggregates leads to a better description of the measured $S(q)$. This may indicate that a SRO order consisting of larger polytetrahedral aggregates (such as dodecahedra) dominates in the undercooled liquid.

The fivefold symmetry of the ISRO is not compatible with the translational symmetry of crystals as they solidify from pure metals. The dissimilarity between SRO in the liquid and the solid may lead to a large interfacial energy, and thus to a large activation energy to form supercritical nuclei. In his early work, Frank has used this argument to explain the large undercoolings,^[20] which have been experimentally observed by application of the volume separation of heterogeneous nucleation sites^[21] and later on by levitation techniques.^[6] On the other hand, if SRO order is similar in liquid and solid, the activation energy for nucleation should be small, and as a consequence undercoolings will be limited and smaller than for pure metals.

Quasicrystal-forming alloys represent a class of solids, which lack long-range translational symmetry of a crystal but show long-range orientational order. The maximum undercoolability of quasicrystal-forming alloys of different degrees of fivefold symmetry has been investigated by levitation experiments. It was found that the higher the degree of fivefold symmetry, the smaller was the undercoolability of the respective alloys.^[22] From this, it is concluded that such alloys will show fivefold SRO in the state of an undercooled melt.

Figure 2 shows, as an example, the partial Bhatia–Thornton structure factor S_{NN} of the quasicrystal-forming $\text{Al}_{13}(\text{Co,Fe})_4$ alloy in the undercooled liquid state measured by elastic neutron scattering. The analysis of the experimental data leads to the conclusion, that, in fact, this alloy shows a topological SRO of fivefold symmetry quite similar to the pure metals.^[23] Consequently, the maximum relative undercoolings $\Delta T_R = T_L - T_N / T_L$ (T_L liquidus and T_N nucleation temperature) of these alloys are by a factor of two smaller than the relative undercoolings of metals.

The situation again changes if glass-forming alloys are studied. Glass formation requires the avoidance of crystal nucleation. It was argued in the literature that the preference of ISRO in the undercooled liquid may favour the glass-forming ability of such alloys.^[24] In fact a series of Zr-based amorphous metals show the primary formation of a fivefold symmetric icosahedral i-phase upon crystallization.^[25–27] However, concerning icosahedral short-range order in the liquid state of Zr-based glass-forming alloys, there is some controversy in the literature. X-ray scattering experiments using

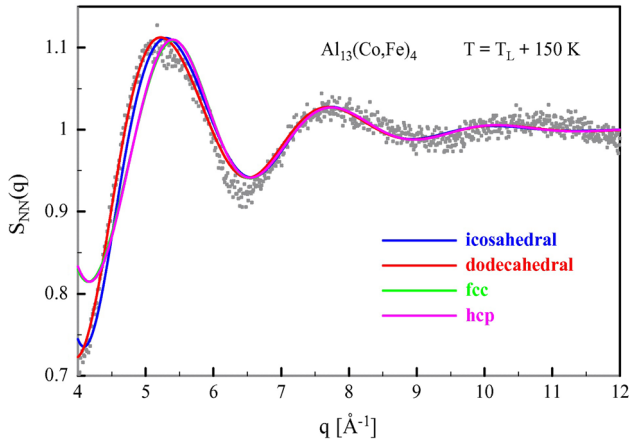


Fig. 2—Structure factor $S(q)$ measured on quasicrystal-forming alloy $\text{Al}_{13}(\text{Fe},\text{Co})_4$ in liquid state. The symbols represent the experimental data, whereas the lines give the results of simulations assuming bcc, fcc, icosahedral, and dodecahedral SRO, respectively (Color figure online).

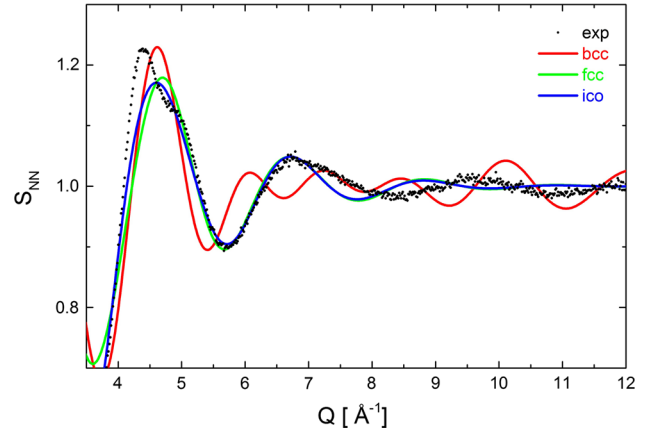


Fig. 3—Structure factor $S(q)$ of liquid Zr_2Pd measured at an undercooling of 250 K (black dots), compared with computed structure factors assuming icosahedral aggregates (blue line), fcc/hcp aggregates (green line), and bcc aggregates (red line) (Color figure online).

high-energy synchrotron radiation on $\text{Zr}_{80}\text{Pt}_{20}$ alloys undercooled by electrostatic levitation reveal a structural factor $S(q)$ that shows a pre-peak and a second peak with a shoulder.^[28]

Figure 3 shows the partial structure factor S_{NN} of a PdZr_2 sample undercooled by 250 K (250 °C). At such a deep undercooling the asymmetry of the second peak is most pronounced. To further analyze the results of the scattering experiments the structure factor S_{NN} was computed assuming fcc/hcp (green line), bcc (red line), and icosahedral structure (blue line). As is obvious from Figure 3 no single structure is able to reproduce the experimentally determined structure factor (black solid line). Therefore, one concludes that the liquid consists of a variety of local structural aggregates. This leads to a frustration effect such that the undercooled melt has no definite pathway in a certain crystalline structure and eventually freezes into the amorphous state. This is quite analogous to spin glasses where ferromagnetic and antiferromagnetic interaction competes with each other and the spin system freezes into a magnetically disordered state.^[29]

B. Crystal Nucleation

It is well known that metallic melts can be undercooled considerably below their respective melting temperatures. By applying containerless processing technologies, heterogeneous nucleation on container walls is completely avoided. If the melt is processed under ultra-high vacuum conditions, contamination of the freely suspended drops can be excluded. The question arises whether under such conditions the maximum degree of undercoolability is achieved as given by the onset of homogeneous nucleation. In contrast to extrinsic heterogeneous nucleation, homogeneous nucleation is an intrinsic process that exclusively depends on physical properties of the material investigated.^[5] To further elaborate this issue, we have investigated the nucleation undercooling statistics of pure Zr processed both by electromagnetic (EML) and electrostatic (ESL) levitation.^[30]

Figure 4 shows the distribution functions of undercoolings measured in the electromagnetic levitator (left) and the electrostatic levitator (right). To analyze the experimental results, we refer to a statistical model developed by Skripov.^[31] According to nucleation theory,^[7] the activation energy ΔG^* for the formation of a nucleus of critical size is given as follows:

$$\Delta G^* = \frac{16}{3} \pi \frac{\sigma^3}{\Delta G_V^2} f(\vartheta), \quad [1]$$

where σ the solid–liquid interfacial energy, $\Delta G_V = G_L - G_S$ the difference of Gibbs free energy per unit volume of liquid G_L and solid G_S , and $f(\vartheta)$ the catalytic potency factor for heterogeneous nucleation with ϑ the wetting angle of the nucleus formed onto a substrate. For pure metals, the driving force for nucleation ΔG_V can be approximated by $\Delta G_V = \Delta S_f \times \Delta T \times V_m^{-1}$ with $\Delta S_f = \Delta H_f \times T_m \Delta S_f$, and ΔH_f the enthalpy of fusion and V_m the molar volume.^[32] The solid–liquid interfacial energy is given by the negentropic model:^[33]

$$\sigma = \alpha \cdot \frac{\Delta S_f \cdot T}{(N_A V_m^2)^{1/3}}, \quad [2]$$

where N_A Avogadro's number and $\alpha = 0.70$ for bcc-structured solid β -Zr that primarily nucleates in the undercooled melt. The steady state nucleation rate, I_{SS} , is computed as follows:^[34]

$$I_{\text{SS}} = K_V \exp\left(-\frac{\Delta G^*}{k_B T}\right) = K_V \exp\left(-\frac{CT^2}{\Delta T^2}\right) \quad [3]$$

with

$$K_V = \frac{k_B T N_o}{3a_o^3 \eta(T)}; C = \frac{16\pi \Delta S_f \alpha^3 f(\vartheta)}{3k_B N_A}, \quad [4]$$

where $\eta(T)$ the temperature dependent viscosity, a_o a typical interatomic spacing, k_B Boltzmann's constant, and N_o the number of potential nucleation sites. For

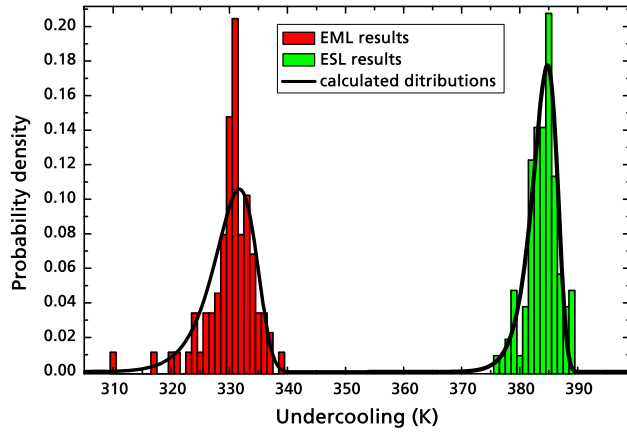


Fig. 4—Probability distributions functions of undercoolings measured in 100 experiment cycles on pure Zr in the electromagnetic (left) and the electrostatic levitator (right). The solid lines give the probability distributions function as computed according to a statistical analysis of nucleation undercooling.

homogeneous nucleation, K_V in Eq. [4] is in the order of magnitude of $K_V \approx 10^{39}/m^3s$ because each atom in the melt can act as a potential nucleation site, $N_o = N_A/V_m$ and the impingement frequency of atoms to the nucleus is assumed to be in the order of the Debye frequency $\approx 10^{13}$ /second. In case of heterogeneous nucleation, only atoms at the catalyzing substrate can act as nucleation site. Therefore, N_o and hence K_V is drastically reduced as compared with homogeneous nucleation.

Nucleation is a stochastic process of rare and independent events. Therefore, the Poisson distribution is applied to determine K_V and C of Eq. [3] from the distribution function of the measured undercoolings. Under non-isothermal conditions (cooling rate $T \neq 0$), the probability ω for one nucleation event in a sample of volume V ($N_n = N_o V$) within the temperature interval T and $T + \delta T$ is given as follows:

$$\omega(1, T + \delta T) = \delta T \frac{VI_{ss}(T)}{|\dot{T}|} \exp \left[- \int_{T_m}^T \frac{VI_{ss}(T)}{\dot{T}} dT \right]. \quad [5]$$

From Eqs. [3–5], the cumulative distribution function $F(T)$ is determined:^[35]

$$F(T) = 1 - \exp \left[- \frac{V}{\dot{T}} \int_{T_m}^T K_V \exp \left(\frac{CT^2}{\Delta T^2} \right) dT \right]. \quad [6]$$

In the present investigations, the temperatures are close to T_m . These temperatures are far away from the glass transition temperature $T_g \approx 0.3 T_m$ of pure metals. Therefore, the temperature dependence of the exponential function containing the activation energy $\Delta G^*(T)$ is much more dominant compared to that of the prefactor of the nucleation rate that is depending on viscosity $\eta(T)$. The temperature dependence of $\eta(T)$ is weak close to T_m but steeply rises if T is approaching T_g . If the temperature dependence of the prefactor is neglected, Eqs. [5] and [6] are simplified as follows:

$$F(T) = 1 - \exp \left[- \frac{VK_V}{\dot{T}d \left(-\frac{\Delta G^*}{k_B T} \right) / dT} \exp \left(\frac{CT^2}{\Delta T^2} \right) dT \right]. \quad [7]$$

According to Eq. [7], a plot of $\ln(-\ln(1 - F(T)))$ vs $T^2/\Delta T^2$ gives a linear relation from which the slope C , and the intercept b are inferred:

$$b = \ln \left[\frac{VK_V}{\dot{T}d \left(-\frac{\Delta G^*}{k_B T} \right) / dT} \right] \quad [8]$$

with

$$\frac{d \left(-\frac{\Delta G^*}{k_B T} \right)}{dT} = 2C \frac{T\Delta T + T^2}{\Delta T^3}. \quad [9]$$

K_V and $\alpha \times f(\vartheta)^{1/3}$ are deduced from C and b . The average relative undercoolings, $\overline{\Delta T}/T_m$, the half width of the distribution functions ω , and the parameters C and b are inferred from the nucleation undercooling analysis.

The functions $\omega(1, T + \delta T)$ are plotted in Figure 4 (solid lines) together with the experimentally determined distribution functions of measured undercoolings (bars). For a direct comparison of both distribution functions measured by EML and ESL, the data have to be normalized with respect to sample size and cooling rate.^[30] The activation energy $\Delta G^*(ESL) = 75k_B T$ and the prefactor $K_V(ESL) = 8 \times 10^{42} m^{-3}s^{-1}$ as inferred from the ESL experiments are much larger than the corresponding values obtained from EML experiments, $\Delta G^*(EML) = 42k_B T$ and the prefactor $K_V(EML) = 8 \times 10^{25} m^{-3}s^{-1}$ as inferred from the EML experiments, respectively. In particular, the prefactor $K_V(ESL) \approx 10^{42} m^{-3} s^{-1}$ is very large in magnitude comparable to a prediction of homogeneous nucleation theory.^[36] If we assume that the maximum undercooling achieved by ESL experiments is approaching the limit of maximum undercooling as set by homogeneous nucleation, a lower limit of the dimensionless interfacial energy α is estimated from the measurements for bcc-structured Zr as $\alpha \sqrt[3]{f(\vartheta)} = 0.61$. This value is larger than predictions by density functional theory, $\alpha = 0.32$,^[37] and MD simulations, $\alpha = 0.48$.^[38] Apparently these models lead to an underestimation of the interfacial energy. The only model in agreement with the present investigations is the negen-tropic model, developed by Spaepen that predicts a value $\alpha = 0.70$ for bcc-structured nuclei.^[33] Later on, Spaepen developed an extended model for the interfacial energy that does take into account also the enthalpic term besides the entropic contribution.^[39] Investigations of bcc vs fcc nucleation in Fe-Ni alloys^[40] and Fe-Ni-Cr steel alloys^[41] and in particular undercooling nucleation investigations on stable and metastable quasicrystalline phases^[42] leads to the conclusion that the enthalpic contribution to the interfacial energy is small compared to the entropic term.

Similar investigations of nucleation undercooling were performed for Co-Pd alloys. At large Co concentrations the deeply undercooled melt shows magnetic ordering in the liquid state. This is indicated by attractive interaction between deeply undercooled $\text{Co}_{80}\text{Pd}_{20}$ alloy and an external strong CoSm magnet,^[43] measurements of the magnetic susceptibility^[44] and muon spin relaxation measurements^[45] on the same alloy. More recent investigations on pure liquid Co processed by the melt fluxing technique in a strong external magnetic field undercooled to 339 K (339 °C) that is only 35 K (35 °C) above the Curie temperature of solid Co. These measurements show the surprising result that the magnetization of the liquid is larger than the magnetization of the solid at the same temperature.^[46] Since the mass density of solid Co is larger than the mass density of liquid Co, one would expect a smaller magnetization of the melt since the interatomic distance is larger and thus, the magnetic interaction should be smaller. However, the situation may be different if the short-range order of undercooled Co melt is considered. Similar as for pure Ni (cf. Figure 1), also undercooled Co melt shows a pronounced icosahedral short-range order.^[47] This means that locally there are atomic arrangements of icosahedral-like aggregates of higher density since an icosahedron is the densest packing of sphere-like elements. Hence, the deeply undercooled Co melt can be considered as a liquid containing icosahedral clusters of high local magnetization randomly distributed in the liquid environment. That is throughout comparable to the ferrofluid systems which consist of ferromagnetic particles dispersed in a non-magnetic carrier fluid.^[48] As a consequence, so-called Rosensweig instabilities are observed for the deeply undercooled Co melt in an external magnetic field,^[46] which are otherwise only known for the ferrofluids.^[49] These instabilities are the result of the balance between free surface tension and the local magnetization and form spikes of the liquid.

Figure 5 shows the phase diagram of the completely miscible Co-Pd alloy with the respective Curie temperatures (upper part) and the prefactors K_V as determined by investigations of the nucleation undercooling statistics (lower part) as a function of the concentration.^[50] The maximum nucleation undercoolings (full circles) are also plotted in the diagram. It can be easily recognized that the measured maximum nucleation undercooling meets the Curie temperature at a concentration of 75 at pct cobalt. At higher Co concentrations, the nucleation undercooling temperature follows the curve of the Curie temperature. From these results, it is concluded that the onset of magnetic ordering may stimulate crystal nucleation.^[51] An explanation for this behavior comes from an estimation of the magnetic contribution to the Gibb's free energy of Co-Pd alloys.^[52]

C. Dendrite Growth

1. Sharp interface theory

Crystal growth in undercooled melts leads to heating up the solid-liquid interface due to the release of the heat of crystallization. As a consequence, a negative

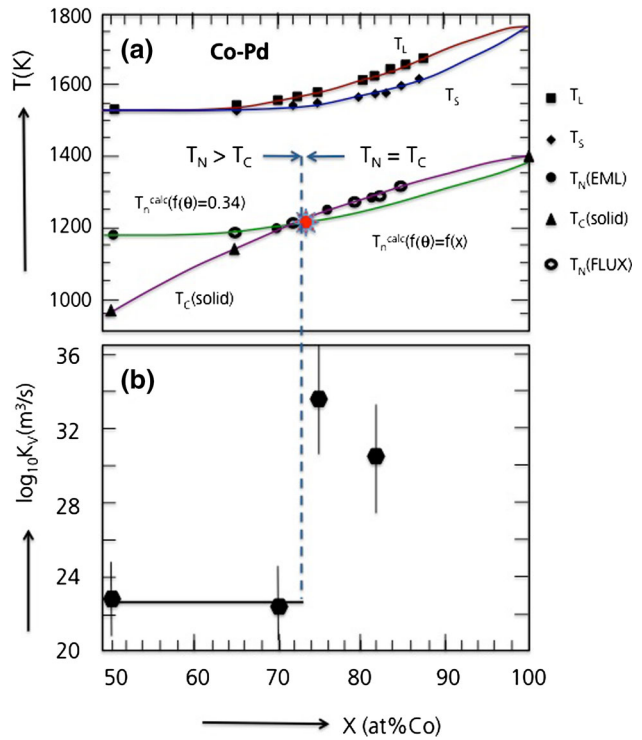


Fig. 5—(a) Co-rich side of the Co-Pd phase diagram. The liquidus (T_L) and solidus (T_S) temperatures as well as the Curie temperatures T_C of solid samples are taken from ref.^[50] The closed and open dots show undercoolings obtained by levitation and fluxing experiments. The diamonds represents undercooling of very small particles (50 μg) of $\text{Co}_{75}\text{Pd}_{25}$ in a duran flux.^[8] The solid line labeled $f(\theta)$ correspond to the prediction of nucleation theory assuming a catalytic potency factor of $f(\theta) = 0.34$. In the regime $X > 75$ at pctCo, the nucleation temperature T_N coincides with the Curie temperature T_C . (b) The prefactor K_V of the nucleation rate as determined by investigations of the nucleation undercooling statistics, it increases by several orders of magnitude if $T_N = T_C$ ^[50] (Color figure online).

temperature gradient will be established in front of the interface since the undercooled melt acts as a heat sink. This will destabilize the initially planar interface. In alloys, a concentration gradient will be built up in addition. Due to limited solubility of the solute in the solid phase, compared to the liquid phase, solute will pile up in front of the interface. The resulting concentration gradient will reinforce, in addition to the negative temperature gradient, the instability of the solidification front. Eventually, the morphological destabilization of an initially planar interface will lead to dendrite growth. Dendrites consist of the main stem and side branches, which grow into the melt.

An extended model of sharp interface theory is applied to describe the growth dynamics of dendrites as a function of undercooling.^[53,54] Accordingly, the total undercooling measured in the experiment is expressed as the sum of various contributions:

$$\Delta T = \Delta T_t + \Delta T_r + \Delta T_n + \Delta T_k + \Delta T_c \quad [10]$$

with ΔT_t the thermal undercooling, ΔT_r the curvature undercooling, ΔT_n the undercooling due to the shift of the equilibrium slope of the liquidus m_E to its non-equilibrium value m_V , ΔT_k the kinetic undercooling,

and ΔT_c the constitutional undercooling, respectively. The thermal undercooling $\Delta T_t = T_i - T_\infty$ with T_i the temperature at the tip of the dendrite and T_∞ the temperature of the undercooled melt far from the interface is expressed as follows:

$$\Delta T_t = \Delta T_{\text{hyp}} I_V(Pe_t) = \frac{\Delta H_f}{C_p^l} I_V(Pe_t), \quad [11]$$

where ΔT_{hyp} is the hypercooling, ΔH_f the heat of fusion, C_p^l the specific heat of the liquid, $I_V(Pe_t) = Pe_t \exp(Pe_t) E_1$ is the Ivantsov function for heat diffusion with $Pe_t = (VR)/2a$ the thermal Peclet number, V the velocity of the tip of the dendrite, R the radius of curvature at the tip of the dendrite, and a the thermal diffusivity. E_1 denotes the first exponential integral function. Due to the strong curvature of the dendrite tip, a reduction of the melting temperature, due to the Gibbs–Thomson effect, has to be taken into account by the curvature undercooling $\Delta T_r = T_L - T_i$ with T_L the liquidus temperature and T_i the temperature at the tip:

$$\Delta T_r = 2\Gamma(1 - 15\varepsilon_s \cos 4\theta)/R, \quad [12]$$

where $\Gamma = \sigma/\Delta S_f$ (σ is interface energy, ΔS_f the entropy of fusion) is the capillary constant (Gibbs–Thomson parameter), ε_s is the parameter of anisotropy of the interface energy, and θ is the angle between the normal to the interface and the direction of growth along the growth-axis. ΔT_n takes into account the change of liquidus line, due to deviations from equilibrium at large dendrite growth velocities, and is expressed as follows:

$$\Delta T_n = (m_E - m_V)c_o, \quad [13]$$

m_E is the slope of liquidus line of the equilibrium phase diagram and m_V is the slope of the liquidus line in the kinetic phase diagram at nominal composition c_o .

The kinetic undercooling ΔT_k is given as follows:

$$\Delta T_k = \frac{V}{\mu}; \quad \mu = \mu_o(1 - \varepsilon_K \cos 4\theta), \quad [14]$$

where μ is the kinetic growth coefficient for growth of the dendrite tip, and ε_K is the parameter of anisotropy for the growth kinetics^[55] and is determined by atomic simulations.^[56] The kinetic undercooling is controlled by the atomic attachment kinetics at the solid–liquid interface that can differ essentially for specific atomic bonding conditions and structural peculiarities. In non-congruently melting alloys, chemical mass transport by segregation has to be considered. The constitutional undercooling in alloys with solidification interval is given by the following equation:

$$\Delta T_c = m_V c_o (k(V) - 1) I_V(Pe_c) / [1 - (1 - k(V)) I_V(Pe_c)], \quad [15]$$

where $Pe_c = (VR)/2D$ is the Peclet number of mass diffusion with D the diffusion coefficient, $I_V(Pe_c) = Pe_c \exp(Pe_c) E_1$ the Ivantsov function for mass diffusion, and $k(V)$ the velocity-dependent partition coefficient. Under the conditions of rapid solidification, for the

range of growth velocity $V < V_D$ (where V_D is the maximum diffusive speed of atoms in the bulk liquid), the liquidus slope is described as follows:^[57]

$$m_V = \frac{m_E}{1 - k_E} \left\{ 1 - k_V + \ln\left(\frac{k_V}{k_E}\right) + (1 - k_V)^2 \frac{V}{V_D} \right\}; \quad V < V_D$$

$$m_V = \frac{m_E \ln k_E}{k_E - 1}; \quad V \geq V_D, \quad [16]$$

where k_E is the partition coefficient of the equilibrium phase diagram. The solute partitioning as a function of growth velocity is described by the non-equilibrium partition coefficient k_V , which becomes dependent on the growth velocity V for the case of rapid solidification^[58]:

$$k_V = \frac{(1 - V^2/V_D^2)[k_E + (1 - k_E)C_o] + V/V_{Di}}{1 - V^2/V_D^2 + V/V_{Di}}; \quad V < V_D$$

$$k_V = 1; \quad V \geq V_D \quad [17]$$

with V_{Di} the interface diffusion velocity obtained by dividing the diffusion coefficient in the solid–liquid interface by the thickness of the interface. The diffusion coefficient in the interface is smaller compared with the bulk diffusion coefficient.^[59]

2. Stability analysis

Equation [12] describes the relation of undercooling in terms of the Peclet numbers, *i.e.*, as a function of the product $V \times R$. For unique determination of the growth velocity V and tip radius R as a function of undercooling, ΔT one needs a second equation for the tip radius R , which comes from stability analysis:

$$R = \frac{\Gamma}{\sigma_o} \left[\frac{\Delta H_f}{C_p^l} Pe_t \xi_t(Pe_T) + \frac{2m_V c_o (k_V - 1)}{1 - (1 - k_V) I_V(Pe_c)} Pe_c \xi_c \right]^{-1}, \quad [18]$$

where ξ_t and ξ_c are the stability functions depending on the thermal and the chemical Peclet number. They are given as follows:

$$\xi_T(Pe_T) = \frac{1}{(1 + a_1 \varepsilon^{1/2} Pe_T)^2},$$

$$\xi_C(Pe_C) = \frac{1}{(1 + a_2 \varepsilon^{1/2} Pe_C)^2},$$

and are defined by the stiffness $\varepsilon = 15\varepsilon_c$ for a crystal with cubic symmetry and with the anisotropy ε_c of the interface energy. The parameters σ_o , a_1 , and a_2 are obtained by fitting to experimental data, or from an asymptotic analysis as described in Reference 60.

Since we are dealing with solidification of electromagnetically levitated drops, forced convection, induced by the strong alternating electromagnetic fields needed to levitate the drop, has to be taken into account. Accordingly, the thermal undercooling $\Delta T_t = T_i - T_\infty$ is expressed as follows:^[61]

$$\Delta T_t = \Delta T_{\text{hyp}} Pe_t \exp(Pe_t + Pe_t^f) \times \int_1^\infty q^{-1} \exp[-qPe_t + (\ln q - q)Pe_t^f], \quad [19]$$

where $Pe_t^f = U_o R / (2a)$ is the flow thermal Péclet number, with U_o the velocity of the uniformly forced flow far from the dendrite tip. We estimate the fluid flow velocity from the energy balance between the electromagnetic field, the gravitational field, and the viscous dissipation:

$$U_o = \left[\frac{2}{\rho} (\rho g R_o) + \frac{B_o^2 (1 - \exp(2 \frac{R_o}{\delta}))}{8\pi} + \frac{\rho \eta^2}{2\delta^2} \right], \quad [20]$$

where g is the modulus of vector of the gravity acceleration, ρ is the mass density, η is the dynamic viscosity of the liquid phase, δ is the skin depth, R_o is the radius of the sample, and B_o is the time-averaged value of the magnetic field inside the levitation coil. Using typical parameters of a metallic system and regarding the boundary conditions of EML experiments, typical fluid flow velocities in liquid metallic drops are determined, ranging in the order of magnitude of several tenths of centimeters per second. This is in agreement with magnetohydrodynamic simulations and experimental observations.^[62]

In case of forced convection inside the melt, the stability parameter σ^* becomes dependent on the fluid flow velocity U_o . It is given as follows:

$$\sigma^* = \sigma_o \varepsilon_c^{7/4} \cdot \left[1 + \chi(Re) \frac{U_o \Gamma}{a \Delta T_{\text{hyp}}} \right], \quad [21]$$

where σ_o is a constant; $Re = U_o R / \nu$ is the Reynolds number. The function $\chi(Re)$ can be found in Reference 63. For computation of the stability parameter, σ^* we choose the results of phase-field modeling^[64] with $\sigma_o \varepsilon_c^{7/4} c / \sigma^* = 1.675$ for the 3D upstream fluid flow imposed on the scale of a freely growing dendrite. Thus, from the two main Eqs. [6] and [14], the velocity V and the tip radius R of the dendrite can be calculated as a function of the initial undercooling ΔT .

Pure metals show in general very large dendrite growth velocities which can range up to 100 m/s at large undercoolings $\Delta T \approx 300$ K (300 °C).^[6] Dendrite growth in pure metals is controlled, exclusively, by heat transport and atomic attachment kinetics at the solid-liquid interface. The curvature undercooling can be neglected since a thermal dendrite has a large curvature radius at its tip compared to alloys. This is caused by the fact that the thermal diffusivity is by orders of magnitude higher than the mass diffusion coefficient in alloys. As a consequence, the total undercooling of a pure metal can be approximated by the sum of thermal and kinetic undercooling, $\Delta T \approx \Delta T_t + \Delta T_k$. At small undercoolings, the thermal undercooling dominates, while at large undercoolings, the kinetic undercooling of the interface becomes dominant. Concerning the interface undercooling, different cases can be distinguished.

According to Coriell and Turnbull, atomic attachment kinetics at the solid-liquid interface of pure metals

should be collision limited.^[65] This means that the atomic vibration frequency, which is in the order of the Debye frequency (10^{13} Hz) in the liquid phase, shall give the limiting factor of atomic attachment kinetics and, therefore, the speed of sound will be the upper limit of growth velocity. Assuming collision-limited growth, the kinetic growth coefficient should be $\mu = 2.77$ m/s/K for pure Ni. Otherwise, atomic simulations of atomic attachment kinetics in pure metals suggest that thermally driven Brownian motion sets the upper limit of atomic attachment kinetics. In this case, the kinetic growth coefficient should be smaller by a factor of 5 to 6, thus, $\mu = 0.5$ m/s/K.^[66]

In the case of diffusion-limited atomic attachment kinetics, the kinetic growth coefficient should be even orders of magnitude smaller compared with collision-limited growth since the relaxation frequency for atomic diffusion is much less than the Debye frequency. Diffusion-limited growth is observed in intermetallic compounds with superlattice crystal structure. In this case, atoms have to sort themselves out to find the proper lattice place. For this process, at least short-range diffusion is necessary. Diffusion-limited growth has been reported first for FeSi and for CoSi equiatomic intermetallic compounds.^[67] Assuming diffusion-controlled attachment kinetics in pure Ni, a kinetic growth coefficient of $\mu = 0.0069$ m/s/K is estimated. For comparison, atomic simulation of kinetic growth coefficients is given, for growth in 100 direction, $\mu_{100} = 0.36$ m/s/K for pure Ni and $\mu_{100} = 0.015$ m/s/K for the equiatomic intermetallic compound AlNi, respectively.^[68] These values are not directly comparable with the figures given above, but reveal, qualitatively, the decrease of the kinetic growth coefficient for collision-limited growth of pure Ni and diffusion-controlled growth for the congruently melting intermetallic compound AlNi.

3. Pure nickel: thermal and kinetic undercooling

Figure 6 exhibits measurements of dendrite growth velocity, V , as a function of undercooling, ΔT , of pure Ni. The open circles represent results of measurements using the capacity proximity sensor (CPS),^[69] the open diamonds give results of measurements using a high-speed camera (HSC).^[14] Both sets of these experiments are performed under terrestrial conditions. In addition, the full squares exhibit results of measurements in reduced gravity using the TEMPUS facility and the HSC.^[70] These results scatter much less compared with the measurements under terrestrial conditions. Obviously, the measured values are significantly smaller in comparison with the CPS data measured under terrestrial conditions. This difference is attributed to the strong convection in electromagnetically levitated melts, which leads to an increase of the growth velocity. The lines represent results of calculations of the dendrite growth velocity within the sharp interface model. The dashed line corresponds to collision-limited growth, the dotted line to thermally controlled growth, the dash-dotted line to diffusion-limited growth, and the solid line is a fit through the high accuracy data obtained in reduced gravity with negligible convection. The kinetic growth coefficient is used as fit parameter and

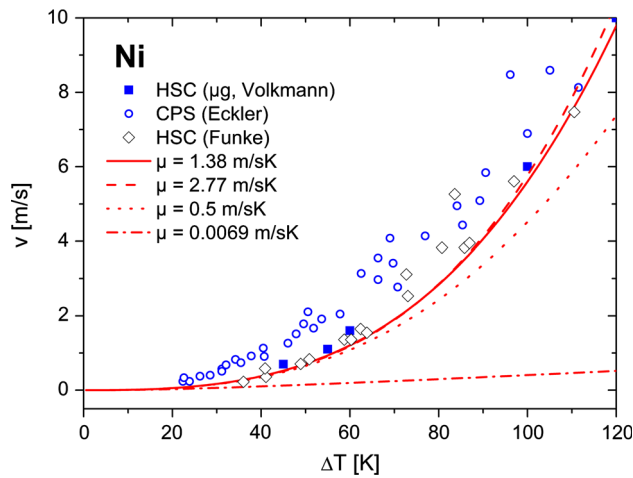


Fig. 6—Dendrite growth velocity V as a function of undercooling ΔT , measured for pure Ni,^[69] using a Capacity Proximity Sensor, CPS (open circles),^[69] a HSC (HSC) in terrestrial experiments (open diamonds)^[14] and a HSC in reduced gravity experiments using the TEMPUS facility during parabolic flight campaigns (full squares).^[70] The lines give the predictions of dendrite growth theory assuming collision-limited growth (dashed), thermally limited growth (dotted), and diffusion-limited growth (dash-dotted). The solid line gives a fit through the results obtained from microgravity experiments in which forced convection is neglected.

yields a value close to the computed value assuming collision-limited growth. From these comparative investigations, it is concluded that the assumption of collision-limited growth leads to a good description of dendrite growth in undercooled nickel.

For the analysis of the data, only measured growth velocity data at undercoolings less than 200 K (200 °C) have been taken into consideration. At this undercooling, a break in the temperature dependence is occurring whose origin is not yet clarified.

4. Dilute Ni-Zr alloy: solute trapping

In alloys, chemical segregation plays an important role in microstructure evolution. This is because the solubility of the solute in the solvent is less in the solid state compared with the liquid state. As a consequence, solute will pile up in front of the solid-liquid interface during solidification under near equilibrium conditions. Only part of the solute can be dissolved in the solid phase with a concentration that is given by the equilibrium phase diagram. However, if the velocity of the growing dendrite is increased and is approaching the atomic diffusive speed, the solute will be trapped in the solid phase with a concentration that is beyond chemical equilibrium. If the growth velocity is exceeding the atomic diffusive speed, the fast growing dendrite stem will trap all solute and partitionless solidification occurs.

Solute trapping during rapid dendrite growth of undercooled melts has been demonstrated in previous investigations of both completely miscible solid solutions, such as Cu-Ni,^[71] and alloys with complex phase diagrams in the region of dilute concentration, such as Ni₉₉B₁ alloy.^[72] This has been further supported by equivalent investigations on the dilute Ni₉₉Zr₁ alloy in which the dendrite growth velocity has been measured

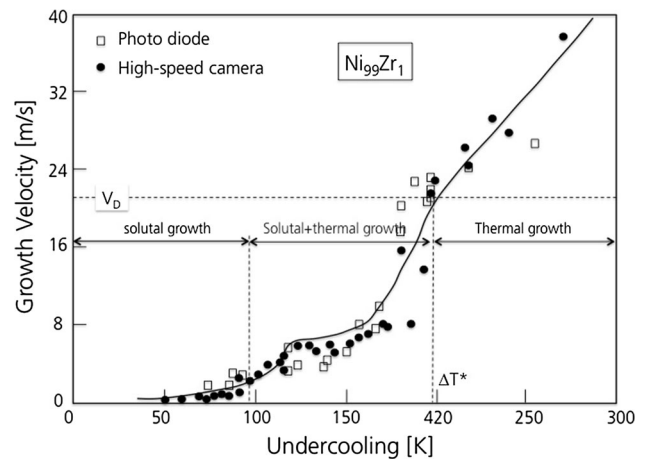


Fig. 7—Theoretical predictions (solid line) of the dendrite growth velocity V vs the undercooling ΔT in comparison with (i) measurements using the Photo Diode technique (open squares) and with (ii) measurements using a High-Speed Camera system (solid circles) for the dilute Ni₉₉Zr₁ alloy. At a critical point $\Delta T(V = V_D) = \Delta T^* = 198$ K, a transition from solutal and thermal growth to purely thermally controlled growth occurs and diffusion-less solidification begins to proceed at $\Delta T(V \geq V_D) \geq \Delta T^*$.

as a function of undercooling using the CPS. The diffusion coefficient, as one of the most important parameter in modeling dendrite growth, was independently determined by laser surface re-solidification experiments in combination with Rutherford backscattering experiments.^[73]

Figure 7 shows the dendrite growth velocity as a function of undercooling measured on Ni₉₉Zr₁, both by the Photo Diode Sensor technique (open symbols) and a HSC (closed symbols), respectively. The solid line represents results of dendrite growth modeling within the sharp interface theory.^[74] The results found using the Photo Diode Sensor technique and the HSC system are matching. Due to methodical and technical improvements, the HSC measurements have lower experimental scatter.

The experimental data on solidification of the Ni₉₉Zr₁ alloy cover a wide range of undercoolings up to $\Delta T = 271$ K and of dendrite growth velocities up to $V = 37.5$ m/s. They clearly exhibit an abrupt change in the solidification mechanism at a fixed critical undercooling ΔT^* , at which the dendrite tip velocity is equal to the solute diffusion speed in bulk liquid, $V = V_D$. The sharp interface model of dendritic growth is used to interpret the experimental results. The model attempts to describe are as follows:

- (i) diffusion-limited growth of dendrites (*i.e.*, growth of “solutal” dendrites at low undercoolings);
- (ii) diffusion-limited and thermally controlled growth of dendrites (*i.e.*, growth of “solutal” and “thermal” dendrites in the intermediate range of undercoolings); and (iii) purely thermally controlled dendritic solidification at higher undercoolings. The description of dendritic growth over the whole range of undercooling is made possible by introducing both deviations from local equilibrium at

the interface, as well as in the solute diffusion field. Both contributions play an important role in high solidification velocities.

It can be seen from Figure 7 that sharp interface theory reasonably predicts three regimes for dendritic solidification in agreement with the experimental data. The first regime is described by the low-velocity branch predicted for chemical diffusion-limited growth. The second regime is transitive, and is characterized by growth of both solutal and thermal dendrites. The third regime occurs at higher undercoolings, consistent with $\Delta T(V) \geq \Delta T^*(V_D)$. This regime begins with an abrupt change in the kinetic curve at $\Delta T = \Delta T^*$, which can be explained by the end of the transition from solutal and thermal dendrites to thermal dendrites and the onset of diffusion-less dendritic growth. The first region ends at an undercooling of about $\Delta T \approx 90$ K. The second region covers the undercooling range $90 \text{ K} < \Delta T < 198$ K, while the third region starts at $\Delta T \approx 198$ K.

An analogous effect to solute trapping, disorder trapping^[55] occurs during rapid crystallization of undercooled melts of *intermetallics* with superlattice structure. In such systems, crystal growth is very sluggish at small undercoolings.^[44] The atomic attachment of atoms from the liquid to the solid needs short-range atomic diffusion, as atoms have to sort themselves out to find their proper lattice place in the superlattice structure. If undercooling increases the non-equilibrium effect of disorder trapping leads to the solidification of a metastable disordered structure.

5. Intermetallic compound $Al_{50}Ni_{50}$: disorder trapping

Measurements of the dendrite growth velocity of intermetallic phases exhibit a steep rise in the growth velocity vs undercooling relation at a critical undercooling ΔT^* . This change of the dendrite growth kinetics has been attributed to a transition from ordered to disordered growth of superlattice structures.^[75-77] However, for $Ni_{50}Al_{50}$ diffraction experiments on the as-solidified samples at ambient temperatures failed to prove a disordered superlattice structure.^[76] This result was explained by transformations of primary solidified disordered structures to stable ordered phases during the post-recalescence and the post-solidification period. It was shown that metastable disordered phases transform to the ordered state on a rather short time scale.^[78] Transmission electron microscopy on rapidly solidified Ni-Al intermetallic alloys reveal antiphase domains, which indicate the occurrence of disorder trapping during crystallization of drop-tube processed melts^[79] and rapid laser surface re-solidification of Ni-Al intermetallic phases.^[80] During pulsed laser melting studies on Ni_3Al , a disordered fcc phase has been quenched in, although an ordered $L1_2$ phase is stable up to the melting temperature, providing indications of disorder trapping during non-equilibrium solidification.^[81] Nevertheless, these studies provide no direct experimental link between the occurrence of disorder trapping and the growth velocity-undercooling relationship.

Figure 8 shows the results of measurements of dendrite growth velocity as a function of undercooling for

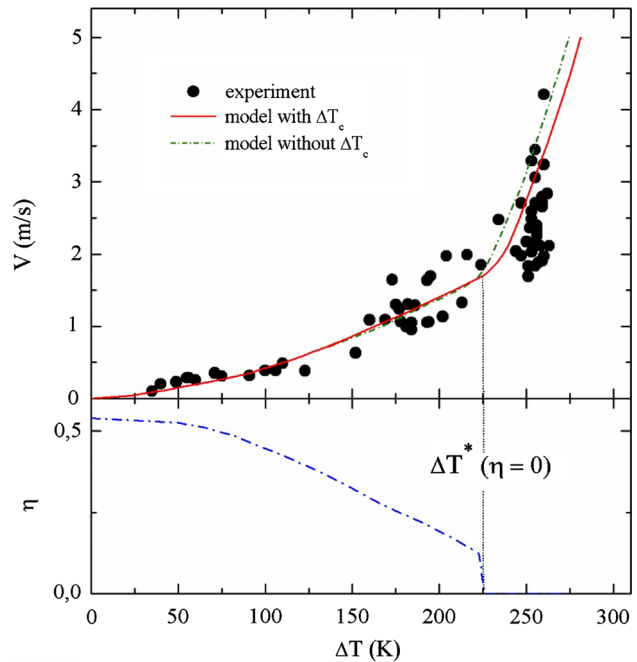


Fig. 8—Top: Dendrite growth velocity V as a function of undercooling ΔT measured by use of a high-speed video camera (full circles) and computed by applying the sharp interface model, with (solid line) and without (dashed-dotted line), taking into account small constitutional effects due to the shift of the congruent melting point in the kinetic phase diagram. If any constitutional contributions are neglected, the temperature characteristics of $V(\Delta T)$ does not change with the exception that the sharp increase of V sets in at a critical undercooling, being about 25 K (25 °C) smaller (dashed-dotted line). Bottom: The order parameter η is shown as a function of undercooling as inferred from the analysis of the experimental results.

the intermetallic $Ni_{50}Al_{50}$ alloy. The measured growth velocities continuously increase with undercooling. If the undercooling exceeds a value of $\Delta T^* \approx 255$ K, a steep rise of V is observed. The intermetallic $Ni_{50}Al_{50}$ alloy melts congruently. Hence, mass transport by mass redistribution and, consequently, constitutional effects can be neglected, therefore, the constitutional undercooling $\Delta T_c \approx 0$. Due to the large curvature radius of thermal dendrites, the curvature undercooling can be equally neglected. Therefore, the thermal undercooling and the kinetic undercooling control the dendrite growth kinetics of the intermetallic $Al_{50}Ni_{50}$ compound.

The results of the measured dendrite growth velocities are analyzed within the sharp interface model. In addition to the system of equations given by this model, the non-equilibrium effect of disorder trapping has to be introduced in this concept. In order to do so, we combine the sharp interface theory with a model of disorder trapping, as developed by Boettinger and Aziz^[82] that has been extended by Assadi and Greer.^[83] This approach bases on the thermodynamic description in which the Gibbs free energy of the liquid, G_L , is expressed by a regular solution model and that of the solid intermetallic phase, G_S , is expressed as a function of the order parameter, η . η is defined by the difference of the fractions of atoms located in the correct and the wrong places within the superlattice of the ordered B2

structure. The link between non-equilibrium thermodynamics and crystal growth is established by three kinetic equations. One of these equations is the growth equation by Wilson and Frenkel:

$$V = V_0 \left(1 - \exp \frac{-\Delta G_{LS}}{k_B T} \right), \quad [22]$$

where $\Delta G_{LS} = G_L - G_S$. The solidification of the congruently melting intermetallic phase of $\text{Ni}_{50}\text{Al}_{50}$ requires no long-range diffusion. Collision-limited growth for the atomic attachment kinetics of atoms from the liquid to the solid is assumed so that the kinetic prefactor V_0 is approximated to be the velocity of sound V_S . For sorting of the atoms on the different sublattices, however, diffusion within the solid–liquid interface is required, which is governed by the speed of interface diffusion V_{DI} and by diffusion in the bulk liquid, V_D , which are two to three orders of magnitude smaller than V_S . The balance of the mass fluxes to the different sublattices of the more or less ordered solid phase during crystal growth defines two other kinetic equations.^[77,82] Apart from thermodynamic and kinetic parameters, the equation system depends on five variables. These are the temperature of the solid–liquid interface T_i , the composition of the solid, c_s , and of the liquid phase, c_l , the order parameter η , and the growth velocity V . For a given V and at a fixed nominal composition of the liquid, c_l , the other three variables, c_s , T_i , and η can be determined by numerically solving the equation system. Hence, the model provides a description for the velocity dependence of the order parameter $\eta(V)$. Moreover, by linking c_l , c_s , and T_i , it allows for calculating a metastable phase diagram in which the liquidus temperature line depends on the velocity V , thus, $T_L(V)$. From this kinetic phase diagram, the kinetic undercooling ΔT_K (difference between local equilibrium liquidus and velocity-dependent liquidus temperature), k_V and m_V are directly inferred. More details of the computations are given in Reference 84.

The results of the computations of dendrite growth velocity as a function of undercooling are given in the upper part of Figure 8 (solid line). It is evident that the predictions of the extended sharp interface model are in reasonable agreement with the experimental results over the entire range of undercooling accessible by application of the EML technique.

At large undercoolings, the model reproduces the sharp increase of V at ΔT^* . Small constitutional effects by the slight shift of the congruent melting point in the kinetic phase diagram are taken into account in the present calculations. If these constitutional effects are neglected, the critical undercooling at which V steeply rises is slightly shifted to lower undercoolings (*cf.* dashed-dotted line in Figure 8). The variation of the order parameter η with undercooling as predicted by the model of disorder trapping^[82] is shown in the lower part of Figure 8. The order parameter continuously decreases with increasing undercooling and drops suddenly to zero at an undercooling at which disorder trapping sets in as indicated by the sharp increase of dendrite growth velocity in the upper part of Figure 8.

Even for small velocities, the order parameter is considerably smaller than 1 because some degree of disorder is favorable at elevated temperatures due to the entropic term in the Gibbs free energy.

6. Intermetallic compound $\text{Al}_{50}\text{Ni}_{50}$: influence of convection

So far, experiments of dendrite growth velocities have been presented which give evidence for various effects of non-equilibrium solidification at large dendrite growth velocities. At moderate and small growth velocities, there will be an influence of convection in heat and mass transport that controls the dendrite growth kinetics. In EML experiments, strong stirring of the melt leads to forced convection. The fluid flow velocity U estimated for such experiments are ranging up to 0.6 m/s. Therefore, one expects an influence of forced convection in the dendrite growth velocity range $V \leq U$.^[85]

$\text{Al}_{50}\text{Ni}_{50}$ was chosen for the investigations on growth kinetics under the conditions of forced convection on Earth and reduced convection in reduced gravity.^[86] This alloy melts congruently and forms an intermetallic B2 β -phase under equilibrium conditions. Crystallization of ordered superlattice structures requires short-range atomic diffusion at the solid–liquid interface. This leads to sluggish growth dynamics, at least as small and intermediate undercoolings (V : 0.1 to 0.5 m/s).^[67] These growth velocities are directly comparable to the speed of fluid flow in levitated metallic melts. Fluid flow motion inside the liquid drop changes the growth dynamics.

This effect, however, will be reduced if the liquid drops are processed in a reduced gravity environment since electromagnetically induced convection and natural convection are much less pronounced. Figure 9 shows the results of measurements of dendrite growth velocity as a function of undercooling for $\text{Al}_{50}\text{Ni}_{50}$ alloy, both under terrestrial conditions (circles) and in reduced gravity (diamonds). All growth velocities measured in reduced gravity are significantly smaller than those determined under terrestrial conditions. At growth velocities exceeding the fluid flow velocity $V > U \approx 0.6$ m/s, data of dendrite growth velocity from terrestrial and from reduced gravity experiments coincide. The results of sharp interface modeling neglecting the influence of fluid flow are depicted in Figure 9 (solid line). It describes the experimental results obtained in reduced gravity. The sharp interface model regarding convection describes the experimental results obtained under terrestrial conditions if a fluid flow velocity, of $U \approx 1.2$ m/s, is assumed (*cf.* dashed line in Figure 9). At growth velocities $V > 0.6$ m/s, the computed relation of $V = f(\Delta T)$, without and with convection, converge to one line since, in this region, the dynamics of solidification is mainly limited by thermal diffusivity.

Convection does not only influence the dendrite growth kinetics but also affects microstructure evolution. A particular interesting finding is observed in measurements of the dendrite growth velocity as a function of undercooling of intermetallic Ni_2B alloy. This alloy system is characterized by a dimensionless entropy of fusion $\Delta S_f/R \approx 2$ (ΔS_f is entropy of fusion, R is gas constant). According to Jackson's rule, such a

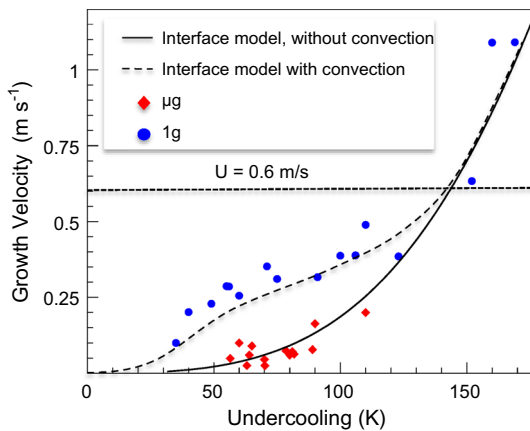


Fig. 9—Dendrite growth velocity of B2 β phase of $\text{Al}_{50}\text{Ni}_{50}$ alloy as a function of undercooling measured under terrestrial conditions (circles) and in reduced gravity (diamonds). The solid line represents the prediction of dendrite growth theory without convection and the dashed line with convection. U denotes the speed of fluid flow inside an electromagnetically levitated droplet as estimated by magnetohydrodynamic simulations^[85].

value of the reduced entropy of fusion is ranging between $\Delta S_f/R = 1$ and $\Delta S_f/R = 3$. $\Delta S_f/R = 1$ is known for metallic systems of more or less isotropic bonding. These systems show a rough interface on the atomic scale and dendritic microstructures on a mesoscopic scale. On the other hand, $\Delta S_f/R = 3$ is known for systems with strong anisotropic bonding as present in covalent systems. These systems show a smooth interface on an atomic scale and faceted microstructures on a mesoscopic scale. Similar as in other intermetallic systems, growth kinetics is sluggish. Therefore, one would expect that convection affects both the growth kinetics and microstructure evolution. We have investigated the solidification of undercooled melt of Ni_2B alloy under different conditions of convection. Different techniques were applied to measure the dendrite growth kinetics as a function of undercooling all of them creating various levels of convection. These are EML on Earth (forced convection), EML in reduced gravity (reduced forced convection), melt fluxing technique (natural convection), melt fluxing in a strong external magnetic field (reduced natural convection), and electrostatic levitation on small samples (almost no convection).^[87]

7. Intermetallic compound Ni_2B : different levels of convection

The Ni_2B dendrite growth velocity along the $\{111\}$ normal directions as a function of undercooling measured under different convective flow conditions is presented in Figure 10. The error bars result from uncertainties in the fitting procedure, *e.g.*, from samples not being perfectly spherical and/or partially hidden by the levitation coil in EML. The growth velocities measured up to $\Delta T_{\text{max}} = 272$ K are well below 1 m/s and are thus comparable with or even less than the expected fluid flow velocities present in 1g EML. The growth velocity $V(\Delta T)$ is found to increase monotonically. As can be seen from Figure 10, for undercoolings $40 \text{ K} < \Delta T < 150 \text{ K}$, the growth velocity increases with

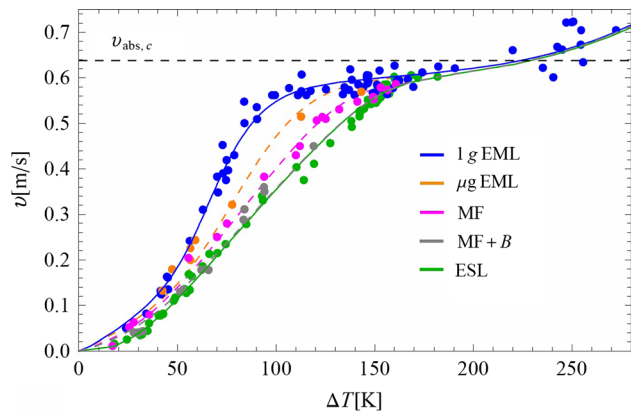


Fig. 10—Dendrite growth velocities as a function of undercooling of Ni_2B alloy for various fluid flow velocities: ESL: $u = 0.00$ m/s, MF + B: $u = 0.01$ m/s, MF: $u = 0.05$ m/s, μg EML: $u = 0.18$ m/s, and 1g EML: $u = 0.25$ m/s (Color figure online).

the fluid flow velocity. The lowest growth velocities are obtained by ESL, followed by the MF and μg EML, whereas the highest values are obtained by 1g EML. Indeed, as soon as convection may play a not negligible role in solidification kinetics, we observed increasing dendrite growth velocity. This is in close agreement with the predicted order of the flow velocities in the various experiment techniques. In the presence of an external static magnetic field of 1.2 Tesla, the growth velocities obtained by MF are slightly shifted to lower values, which, within the limit of accuracy, overlap with the ESL values. Deviations may be due to the influence of residual flow that is not completely stabilized by the magnetic field. Interestingly, the results obtained by μg EML are quite close to the velocities measured under the condition of natural convection in MF.

For $\Delta T < 40$ K as well as $\Delta T \geq 150$ K, the data coincide within the uncertainty of the measurements. This is physically reasonable since, on the one hand, the growth velocity must vanish for $\Delta T = 0$ K and, on the other hand, the influence of convection is likely to become less pronounced in the high-velocity region. The difference in the growth velocities in the medium undercooling range is due to an apparent change in the slope of the 1g EML $V(\Delta T)$ data measured under the condition of forced convection. This results in a significant gap of roughly 60 pct at $\Delta T \approx 100$ K between the ESL and 1g EML data of growth velocities, which may be attributed to an enhanced heat and mass transfer due to electromagnetically induced convection.

For the further analysis, we apply the sharp interface model taking into account heat transport by convection similar as in case of the $\text{Al}_{50}\text{Ni}_{50}$ alloy. But surprisingly, this does not lead to a reproduction of the experimental results. Also taking into account the small shifts in the concentration from the stoichiometric composition of Ni_2B alloy which may occur during the processing the samples at high temperatures due to evaporation is not satisfactory.

Growth in Ni_2B is predominantly governed by the kinetic contribution to the total undercooling. The kinetic undercooling is governed by atomic attachment

kinetics at the solid–liquid interface. It depends very much on the interface morphology. In general, it can be categorized either as atomically smooth (faceted) or atomically diffuse (rough). In the first case, the solid–liquid interface is thin, in the order of one atomic layer, while in the second case the interface is rather diffuse over several atomic layers. According to Jackson, the atomic arrangement at the interface depends mainly on the entropy of fusion ΔS_f .^[88] If the dimensionless entropy $\Delta S_f/R_G < 2$ (R_G is gas constant), then a rough interface will be favored, while for $\Delta S_f/R_G > 2$ a smooth interface will be preferentially formed.^[89] Pure metals are often characterized by $\Delta S_f \approx R_G$ and are predicted to have a rough interface. However, many intermetallic compounds show high entropy of fusion due to strong chemical bonding and, consequently, a smooth faceted interface will be formed. Faceted interfaces have inherently a low accommodation factor $f < 1$ in contrast to $f = 1$ for metals. This means not each atomic jump from the liquid to the solid will be successful. In such a case, the interface undercooling as given in Eq. [10] can be written as follows:^[90]

$$\Delta T_k = \left(\frac{V}{\mu}\right)^n, \quad [23]$$

where the kinetic exponent n is determined from experiments. The 1g EML results can be reproduced much more accurately by setting $n < 1$. For pure faceted

Table I. Best Fit Parameters Used to Calculate the Ni₂B Growth Velocities as Shown in Fig. 10

Parameters	Value		
	Stability Parameter σ^*	Fluid Flow Velocity u (m/s)	Kinetic Exponent n
1g EML	5.0×10^{-5}	0.25	0.85
μ g EML	7.0×10^{-5}	0.18	0.93
MF	9.0×10^{-5}	0.05	0.98
MF + B	1.0×10^{-4}	0.01	1.00
ESL	1.0×10^{-4}	0.00	1.00

The kinetic growth coefficient μ is obtained for $f \times v_s = 4.25$ m/s.

spiral growth, $n = 0.5$.^[91] It is found that the increase in growth velocity, as observed in 1g EML, is only partly due to the influence of electromagnetically driven flow on the thermal and solute concentration fields in front of the solid–liquid interface but can be mainly attributed to the substantial change in growth kinetics caused by a convection induced transition from dendrites to more faceted solidification structures, shown in Table I.

This change is supported by investigating the microstructures of samples solidified upon undercooling in ESL and EML. Figure 11(b) displays the microstructure of a sample solidified under the condition of no convection (ESL), while Figure 10b gives the structure

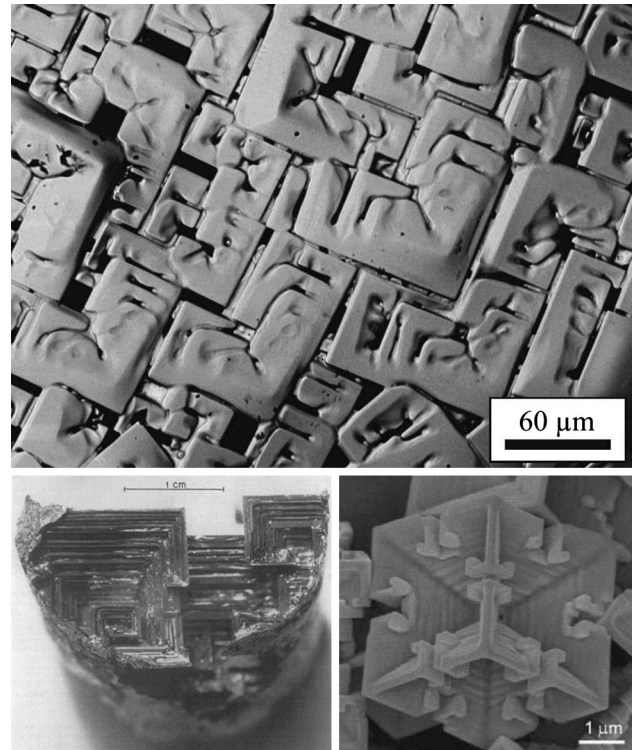


Fig. 12—Top: The structure of the Ni₂B—rod-like morphology solidified under the conditions of forced convection (EML); bottom: hopper crystals found in Bi (left)^[94] and PbTe, (right)^[93].

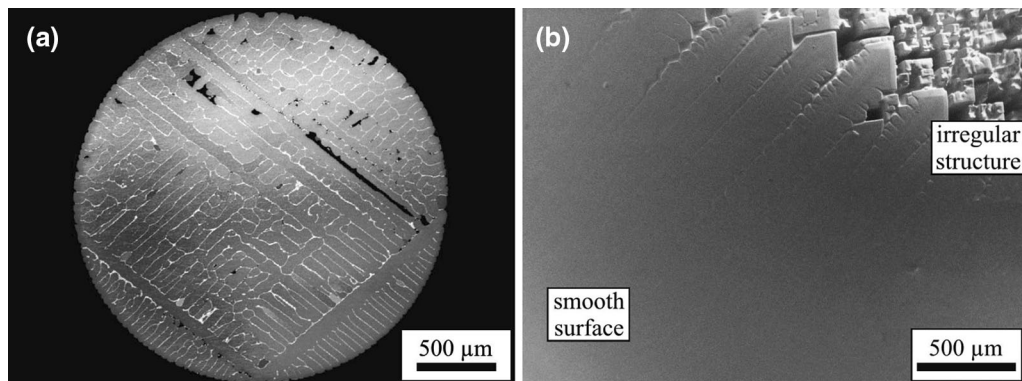


Fig. 11—(a) Dendritic structure of a sample solidified without convection (ESL). Growth direction is perpendicular to {111}. (b) Structure of a sample solidified with forced convection (EML). Growth direction is along [001].

of a sample solidified under the conditions of forced convection (EML).^[92] Samples processed in ESL exhibit the regular dendritic pattern. In contrast, the smooth structure of samples processed in EML shows a transition to irregular rod-shaped structures. This change is not associated with a change of crystallographic phase as proven by EBSD. Apparently, the internal structure resembles the well-known morphology of so-called Hopper crystals, which are rarely found for metallic materials but are often observed in non-metallic systems. The structure found in Ni₂B processed in EML under the conditions of forced convection is compared to Bi and PbTe hopper crystals in Figure 12.

A hopper crystal, also termed “skeleton” of a crystal, is usually formed due to a disparity of growth rates, *i.e.*, the crystal edges are growing more rapidly than the crystal faces. This is a typical example of faceted growth on a more local level.^[94] Hopper crystals have been reported for non-metallic forsterite (Mg₂SiO₄)^[95] and PbS single crystals.^[96] Faceted growth is expected in systems of high entropy of fusion ΔS_f , as *e.g.*, in Bi, $\Delta S_f = 2.4 R_G$. This is larger than $\Delta S_f = 2 R_G$ as in the present case of Ni₂B. Obviously, forced convection induces faceting of the solid–liquid interface in systems, which show otherwise the growth of a rough solid–liquid interface of metallic systems.

IV. CONCLUSIONS

Containerless processing by electromagnetic and electrostatic levitation has been applied to investigate topological and magnetic order in undercooled metallic melts. Crystal nucleation and rapid dendrite growth in undercooled melts of pure zirconium and pure nickel, and various binary metallic alloys have been studied. Very large undercoolings were achieved. A statistical analysis of the distribution function of maximum undercoolings in electrostatic levitation experiments hints to the onset of homogeneous nucleation in undercooled Zr-melts. From the homogeneous nucleation rate calculated within classical nucleation theory, a lower limit of the solid–liquid interfacial energy was deduced. This value indicates that results by density functional theory and molecular dynamics simulations may lead to an underestimation of the solid–liquid interfacial energies.

Dendrite growth kinetics was studied in detail at very large undercoolings. Non-equilibrium effects have been detected by measurements of the dendrite growth velocity as a function of undercooling. In dilute Ni₉₉Zr₁ alloy, a critical undercooling was identified at which a transition from chemically to pure thermally controlled growth is observed. As evidenced by neutron auto-radiography investigations on a similar dilute alloy, Ni₉₉B₁, it was demonstrated that this transition is accompanied by complete partitionless solidification leading to a metastable supersaturated solution. A similar phenomenon, disorder trapping was studied by undercooling experiments on the intermetallic compound Al₅₀Ni₅₀. By measurements of the dendrite growth velocity of the equiatomic Al₅₀Ni₅₀ alloy at very

large undercoolings, a transition from ordered to disordered growth of the B2 β -phase was identified. In case of solid solutions, solute trapping was identified to set in at a critical undercooling. Analogous to solute trapping, disorder trapping in intermetallic compounds is evidenced at a critical undercooling at which the dendrite growth velocity steeply rises similar as in case of solute trapping in solid solutions.

Comparative experiments on Earth, and in reduced gravity, of measurements of dendrite growth in undercooled Al₅₀Ni₅₀ clearly reveal the importance of forced convection on growth dynamics, which has to be taken into account to predict growth dynamics in undercooled melts. By taking into account a velocity-dependent order parameter, dendrite growth theory was extended such that it describes quantitatively the dendrite growth velocity over the entire undercooling range accessible by containerless processing and reproducing the transition from ordered to disordered growth. This leads to the solidification of a metastable disordered superlattice structure of the intermetallic compound. Finally, investigations of both dendrite growth kinetics and microstructure evolution on the intermetallic compound Ni₂B give evidence that forced convection leads to a transition from dendrite-like growth to faceted growth.

All of these investigations prove containerless processing to be a powerful experimental tool to investigate phenomena of solidification, which are far away from equilibrium. They lead to various solid metastable materials. Hence, undercooling is an efficient parameter to control phase selection during solidification.

ACKNOWLEDGMENTS

The authors thank former colleagues Oliver Heinen, Helena Hartmann, Dieter Platzek, and Thomas Schenk for excellent cooperation and fruitful discussions. Financial support by Deutsche Forschungsgemeinschaft within contracts HE1601/18, HE1601/21, HE1601/25, HE1601/26, DLR Space Agency within contract 50WM1140, and the European Space Agency within contract 15236/02/NL/SH is gratefully acknowledged.

REFERENCES

1. D. Turnbull: *J. Appl. Phys.*, 1950, vol. 21, pp. 1022–29.
2. J.H. Perepezko: *Mater. Sci. Eng.*, 1984, vol. 65, pp. 125–34.
3. H.W. Kui, A.L. Greer, and D. Turnbull: *Appl. Phys. Lett.*, 1984, vol. 45, pp. 615–18.
4. F. Gillissen, D.M. Herlach, and B. Feuerbacher: *Zeitschrift für Physikalische Chemie*, 1988, vol. 156, pp. 129–36.
5. D.M. Herlach, R.F. Cochrane, I. Egry, H.-J. Fecht, and A.L. Greer: *Int. Mater. Rev.*, 1993, vol. 6, pp. 273–347.
6. D.M. Herlach: *Annu. Rev. Mater. Sci.*, 1991, vol. 21, pp. 23–92.
7. W.-K. Rhim, S.K. Chung, D. Barber, K.F. Man, G. Gutt, A.J. Rulison, and R.E. Spjut: *Rev. Sci. Instrum.*, 1993, vol. 64, pp. 2961–70.
8. T. Meister, H. Werner, G. Lohoefer, D.M. Herlach, and H. Unbehauen: *Eng. Pract.*, 2003, vol. 11, pp. 117–28.
9. C. Notthoff, H. Franz, M. Hanfland, D.M. Herlach, D. Holland-Moritz, and W. Petry: *Rev. Sci. Instrum.*, 2000, vol. 71, pp. 3791–96.

10. O. Shuleshova, W. Löser, D. Holland-Moritz, D.M. Herlach, and J. Eckert: *J. Mater. Sci.*, 2012, vol. 47, pp. 4497–4513.
11. T. Schenk, D. Holland-Moritz, V. Simonet, R. Bellissent, and D.M. Herlach: *Phys. Rev. Lett.*, 2002, vol. 89, pp. 075507-1–5.
12. K.F. Kelton, G.W. Lee, A.K. Gangopadhyay, R.W. Hyers, T. Rathz, J. Rogers, M.B. Robinson, and D. Robinson: *Phys. Rev. Lett.*, 2003, vol. 90, pp. 195504-1–6.
13. K.F. Kelton, A.L. Greer, D.M. Herlach, and D. Holland-Moritz: *Mater. Res. Bull.*, 2004, vol. 29, pp. 940–65.
14. O. Funke, G. Phanikumar, P.K. Galenko, L. Chernova, S. Reutzel, M. Kolbe, and D.M. Herlach: *J. Cryst. Growth*, 2006, vol. 297, pp. 211–22.
15. D.M. Herlach and D.M. Matson eds.: *Solidification of Containerless Undercooled Melts*, Wiley, Weinheim, 2012.
16. J. Piller, R. Knauf, P. Preu, D.M. Herlach, G. Lohöfer: *ESA 1986, SP-256*, pp. 437–46.
17. D. Holland-Moritz, T. Schenk, R. Bellissent, V. Simonet, K. Funakoshi, J.M. Merino, Buslaps, and S. Reutzel: *J. Non-Cryst. Solids*, 2002, vols. 312–314, pp. 47–56.
18. S. Sachdev and D.R. Nelson: *Phys. Rev. Lett.*, 1984, vol. 53, pp. 1947–53.
19. V. Simonet, F. Hippert, H. Klein, M. Audier, R. Bellissent, H. Fischer, A.P. Murani, and D. Boursier: *Phys. Rev. B*, 1998, vol. 58, pp. 6273–86.
20. F.C. Frank: *Proc. R. Soc. Lond A*, 1952, vol. 215, pp. 43–46.
21. D. Turnbull: *J. Appl. Phys.*, 1950, vol. 21, pp. 1022–28.
22. D. Holland-Moritz, D.M. Herlach, and K. Urban: *Phys. Rev. Lett.*, 1993, vol. 71, pp. 1196–99.
23. T. Schenk, V. Simonet, D. Holland-Moritz, R. Bellissent, T. Hansen, P. Convert, and D.M. Herlach: *Europhys. Lett.*, 2004, vol. 65, pp. 34–40.
24. H. Tanaka: *J. Phys.*, 2003, vol. 15, pp. L491–98.
25. A. Inoue, T. Zhang, J. Saida, M. Matsushita, M.W. Chen, and T. Sakurai: *Mater. Trans. Jpn. Inst. Met.*, 1999, vol. 40, pp. 1181–88.
26. U. Köster, J. Meinhardt, S. Roos, and H. Liebertz: *Appl. Phys. Lett.*, 1996, vol. 69, pp. 179–81.
27. L.Q. Xing, J. Eckert, W. Löser, and L. Schultz: *Appl. Phys. Lett.*, 1999, vol. 74, pp. 664–66.
28. N.A. Mauro, V. Wessels, J.C. Bendert, S. Klein, A.K. Gangopadhyay, M.J. Kramer, S.G. Hao, G.E. Rustan, A. Kreyssig, A.I. Goldman, and K.F. Kelton: *Phys. Rev. B*, 2011, vol. 83, pp. 184109-1–11.
29. C.Y. Huang: *J. Magn. Magn. Mat.*, 1985, vol. 51, pp. 1–74.
30. S. Klein, D. Holland-Moritz, and D.M. Herlach: *Phys. Rev. B (BR)*, 2009, vol. 80, pp. 212202-1–4.
31. V.P. Skripov: *Material Science, Crystal Growth and Materials*, North Holland, Amsterdam, 1977.
32. D. Turnbull: *J. Appl. Phys.*, 1950, vol. 21, pp. 1022–31.
33. D.R. Nelson and F. Spaepen: *Solid State Phys.*, Academic, New York, 1989.
34. D. Turnbull: *Contemp. Phys.*, 1969, vol. 10, pp. 473–96.
35. W.H. Hofmeister, C.W. Morton, R.J. Bayuzick, A.J. Rulison, and J.L. Watkins: *Acta Mater.*, 1998, vol. 46, pp. 6033–39.
36. J.A. Dantzig and M. Rappaz: *Solidification* EPFL Press, Lausanne, 2009.
37. D.W. Marr and A.P. Gast: *J. Chem. Phys.*, 1993, vol. 99, pp. 2024–31.
38. D.Y. Sun, M. Asta, and J.J. Hoyt: *Phys. Rev. B*, 2004, vol. 69, pp. 024108-1–11.
39. F. Spaepen: *Solid State Physics*, 1994, vol. 47, pp. 1–32.
40. E. Schleip, D.M. Herlach, and B. Feuerbacher: *Europhys. Lett.*, 1990, vol. 11, pp. 751–55.
41. W. Löser and D.M. Herlach: *Metall. Trans. A*, 1992, vol. 23, pp. 1585–91.
42. D. Holland-Moritz, J. Schroers, D.M. Herlach, B. Grushko, and K. Urban: *Acta Mater.*, 1998, vol. 46, pp. 1601–15.
43. D. Platzek, C. Notthoff, D.M. Herlach, G. Jacobs, D. Herlach, and K. Maier: *Appl. Phys. Lett.*, 1994, vol. 65, pp. 1723–24.
44. J. Reske, D.M. Herlach, F. Keuser, K. Maier, and D. Platzek: *Phys. Rev. Lett.*, 1995, vol. 75, pp. 737–39.
45. D. Herlach, C. Bührer, D.M. Herlach, K. Maier, C. Notthoff, and D. Platzek: *J. Reske Europhys. Lett.*, 1998, vol. 44, pp. 98–104.
46. J. Wang, J. Li, R. Hu, and E. Bagnon: Private Communication and tbp.
47. D. Holland-Moritz, T. Schenk, R. Bellissent, V. Simonet, K. Funakoshi, J.M. Merino, T. Buslaps, and S. Reutzel: *J. Non-Cryst. Solids*, 2002, vols. 312–314, pp. 47–51.
48. M. Cowley and R.E. Rosensweig: *J. Fluid Mech.*, 1967, vol. 30, pp. 671–88.
49. R.E. Rosensweig: *Annu. Rev. Fluid Mech.*, 1987, vol. 19, pp. 437–61.
50. T. Schenk, D. Holland-Moritz, and D.M. Herlach: *Europhys. Lett.*, 2002, vol. 50, pp. 402–408.
51. D.M. Herlach, D. Holland-Moritz, T. Schenk, K. Schneider, G. Wilde, O. Boni, J. Fransaer, and F. Spaepen: *J. Non-Cryst. Solids*, 1999, vols. 250–252, pp. 271–76.
52. D. Holland-Moritz and F. Spaepen: *Philos. Mag.*, 2004, vol. 84, pp. 957–66.
53. P.K. Galenko and S. Sobolev: *Phys. Rev. E*, 1997, vol. 55, pp. 343–52.
54. P.K. Galenko and D.A. Danilov: *Phys. Lett. A*, 1997, vol. 235, pp. 271–78.
55. E. Brener and V.I. Melnikov: *Adv. Phys.*, 1991, vol. 40, pp. 53–97.
56. J.J. Hoyt, M. Asta, and A. Karma: *Phys. Rev. Lett.*, 2001, vol. 86, pp. 5530–33.
57. P. Galenko: *Phys. Rev. B*, 2002, vol. 65, pp. 144103-1–8.
58. P. Galenko: *Phys. Rev. E*, 2007, vol. 76, pp. 031606-1–9.
59. A. Kerrache, J. Horbach, and K. Binder: *Europhys. Lett.*, 2008, vol. 81, pp. 58001-1–6.
60. D.V. Alexandrov and P.K. Galenko: *Phys. Rev. E*, 2013, vol. 87, pp. 062403-1–5.
61. D.M. Herlach and P.K. Galenko: *Mater. Sci. Eng., A*, 2007, vols. 449–451, pp. 34–41.
62. J. Lee, D.M. Matson, S. Binder, M. Kolbe, D.M. Herlach, and R.W. Hyers: *Metall. Mater. Trans. B*, 2013, vol. 44B, pp. 11663-013-9995-5.
63. P. Bouissou and P. Pelce: *Phys. Rev. A*, 1989, vol. 40, pp. 6673–80.
64. J.-H. Jeong, N. Goldenfeld, and J.A. Danzig: *Phys. Rev. E*, 2001, vol. 64, pp. 041602-1–14.
65. S.R. Coriell and D. Turnbull: *Acta Metall.*, 1982, vol. 30, pp. 2135–39.
66. J.J. Hoyt, M. Asta, T. Haxhimali, A. Karma, R.E. Napolitano, R. Trivedi, B.B. Laird, and J.R. Morris: *Mater. Res. Soc. Bull.*, 2004, vol. 12, pp. 935–39.
67. M. Barth, B. Wei, and D.M. Herlach: *Phys. Rev. B*, 1995, vol. 51, pp. 3422–28.
68. R.E. Rozas, P. Kuhn, J. Horbach: in *Solidification of Containerless Undercooled Melts*; D.M. Herlach and D.M. Matson, eds., Wiley, Weinheim, Germany, 2012, pp. 381–401.
69. K. Eckler and D.M. Herlach: *Mater. Sci. Eng., A*, 1994, vol. 178, pp. 159–62.
70. T. Volkmann: unpublished results.
71. R. Willnecker, D.M. Herlach, and B. Feuerbacher: *Phys. Rev. Lett.*, 1989, vol. 62, pp. 2707–710.
72. K. Eckler, R.F. Cochrane, D.M. Herlach, B. Feuerbacher, and M. Jurisch: *Phys. Rev. B Brief Rep.*, 1992, vol. 45, pp. 5019–22.
73. C.B. Arnold, M.J. Aziz, M. Schwarz, and D.M. Herlach: *Phys. Rev. B*, 1999, vol. 59, pp. 334–43.
74. P.K. Galenko, S. Reutzel, D.M. Herlach, D. Danilov, and B. Nestler: *Acta Mater.*, 2007, vol. 55, pp. 6834–42.
75. M.J. Aziz and W.J. Boettinger: *Acta Metall. Mater.*, 1994, vol. 42, pp. 527–37.
76. P. Gandham, K. Biswas, O. Funke, D. Holland-Moritz, D.M. Herlach, and K. Chattopadhyay: *Acta Mater.*, 2005, vol. 53, pp. 3591–600.
77. H. Assadi, S. Reutzel, and D.M. Herlach: *Acta Mater.*, 2006, vol. 54, pp. 2793–800.
78. M. Sutton, Y.S. Yang, J. Mainville, J.L. Jordan-Sweet, K.F. Ludwig, and G.B. Stephenson: *Phys. Rev. Lett.*, 1989, vol. 62, pp. 288–91.
79. A.L. Greer and H. Assadi: *Mater. Sci. Eng. A*, 1997, vols. 226–228, pp. 133–41.
80. W.J. Boettinger, L.A. Bendersky, J. Cline, J.A. West, and M.J. Aziz: *Mater. Sci. Eng. A*, 1991, vol. 133, pp. 592–95.
81. Y. Huang, M.J. Aziz, J.W. Hutchinson, A.G. Evans, R. Saha, and W.D. Nix: *Acta Mater.*, 2001, vol. 49, pp. 2853–61.
82. W.J. Boettinger and M.J. Aziz: *Acta Metall.*, 1989, vol. 37, pp. 3379–91.

83. H. Assadi and A.L. Greer: *J. Cryst. Growth*, 1997, vol. 172, pp. 249–58.
84. H. Hartmann, D. Holland-Moritz, P.K. Galenko, and D.M. Herlach: *Europhys. Lett.*, 2009, vol. 87, pp. 40007-1–6.
85. R.W. Hyers: *Meas. Sci. Technol.*, 2005, vol. 16, pp. 394–401.
86. S. Reutzel, H. Hartmann, P.K. Galenko, S. Schneider, and D.M. Herlach: *Appl. Phys. Lett.*, 2007, vol. 91, pp. 041913-1–3.
87. S. Binder, P.K. Galenko, and D.M. Herlach: *J. Appl. Phys.*, 2014, vol. 115, pp. 05351-1–11.
88. K.A. Jackson: *J. Cryst. Growth*, 1974, vols. 24–25, pp. 130–36.
89. M.E. Glicksman and R.J. Schaefer: *J. Cryst. Growth*, 1967, vol. 1, pp. 297–310.
90. J.A. Dantzig and M. Rappaz: *Solidification (Engineering Sciences Materials)*, EPFL Press, Lausanne, 2009.
91. D.A. Porter, and K.E. Easterling: *Phase Transformations in Metals and Alloys*, Chapman and Hall, London, 1992.
92. S. Binder, P.K. Galenko, and D.M. Herlach: *Phil. Mag. Lett.*, 2013, vol. 93, pp. 608–17.
93. S. Binder: PhD Thesis, Ruhr-University Bochum 2009.
94. K.A. Jackson, D.R. Uhlmann, and J.D. Hunt: *J. Cryst. Growth*, 1967, vol. 1, pp. 1–36.
95. F. Faure, G. Trolliard, C. Nicollet, and J.-M. Montel: *Contrib. Mineral. Petrol.*, 2003, vol. 145, pp. 251–68.
96. J.M. Garcia-Ruiz: *J. Cryst. Growth*, 1986, vol. 75, pp. 441–53.